Computers in Biology and Medicine 111 (2019) 103341

Contents lists available at ScienceDirect

Computers in Biology and Medicine

journal homepage: www.elsevier.com/locate/compbiomed

Left atrial imaging and registration of fibrosis with conduction voltages using LGE-MRI and electroanatomical mapping

Jinny Lee (이지은)[a,b], Rebecca E. Thornhill[c], Pablo Nery[b], Robert deKemp[b], Elena Peña[c], David Birnie[c], Andy Adler[a], Eranga Ukwatta[a,d,*]

[a] Department of Systems and Computer Engineering, Carleton University, 1125, Colonel By Drive, Ottawa, ON, Canada, K1S 5B6
[b] The University of Ottawa Heart Institute, 40 Ruskin St., Ottawa, ON, K1Y 4W7, Canada
[c] The Ottawa Hospital, 1053 Carling Ave, Ottawa, ON, K1H 8L6, Canada
[d] School of Engineering, University of Guelph, 50 Stone Rd E., Guelph, ON, N1G 2W1, Canada

ARTICLE INFO

Keywords:
Atrial fibrillation
Electroanatomical voltage mapping system
Late gadolinium enhancement magnetic resonance imaging
Point cloud registration
Non-rigid iterative closest point

ABSTRACT

Background and purpose: Abnormal electrical conduction and excitability associated with fibrosis in the left atrium (LA) may serve as a substrate for atrial fibrillation (AF). Electroanatomical voltage mapping systems (EAMs) have become a dominant facilitator to treat AF with catheter ablation assisted by additional diagnostic imaging modalities. Importantly, AF has been associated with structural changes to the extracellular matrix of the myocardium, including increased collagen deposition—a process known as fibrosis. Late gadolinium enhancement-magnetic resonance imaging (LGE-MRI) may aid in guiding AF cardiac ablation therapy by determination of location of fibrosis in the LA. To locate fibrosis for cardiac ablation, however, accurate registration between EAMs and LGE-MRI data is crucial. The purpose of this work was to develop a method for registering EAMs with late gadolinium enhancement-magnetic resonance (LGE-MR) images of fibrosis.

Methods: Twenty patients with persistent AF, who underwent magnetic resonance imaging scanning and EAMs prior to first-time catheter ablation, participated in the study. In our registration pipeline, LGE-MR images were registered to the left atrial surface on EAMs using manual alignment followed by iterative closest point (ICP), and non-rigid ICP (NICP) algorithm.

Results and conclusions: The results demonstrate that NICP provided a substantial reduction in registration error when compared to the use of affine ICP alone. Regions of fibrosis on LGE-MR images identified using the signal threshold to reference mean threshold demonstrated the most regional overlap with low bipolar voltage points on EAMs. Successful co-registration of LGE-MR images to EAMs may assist electro-physiologists in selecting candidate targets for ablation and ultimately, reduce the rate of AF recurrence for patients.

1. Introduction

Atrial Fibrillation (AF) is a heart rhythm disorder of the left atrium (LA) that is associated with an increased risk of stroke and death. A 2010 study estimated that 2.7 to 6.1 million people in the United States suffer from AF, and this number is expected to increase to 12.1 million in 2030 [1]. AF can be classified as paroxysmal, persistent, and longstanding persistent (also known as ‘permanent’ AF) [2]. While catheter ablation is highly successful for most patients with paroxysmal AF, it is much less effective for patients with persistent and longstanding persistent AF [3]. Despite advancements in catheter ablation technology, its success rate remains as low as 45–50% after treatment [4]. These considerable treatment challenges have motivated a number of experimental studies, including some that explored the correlation between the extent of fibrillation burden and the degree of fibrosis in the LA [5,6]. Importantly, AF has been associated with structural changes to the extracellular matrix of the myocardium, including collagen deposition—a process known as fibrosis. For example, Verma [7] showed that patients with evidence of fibrosis in the LA at the time of ablation resulted in nearly half the success rate of those without (43 *vs.* 81%).

Electroanatomical voltage mapping systems (EAMs) can identify the presence, location, and extent of fibrosis in the LA by detection of abnormally conductive or ‘low voltage’ tissue regions [8]. These systems enable operators to position the catheters without fluoroscopic

---

[*] Corresponding author. Department of Systems and Computer Engineering, Carleton University, 1125, Colonel By Drive, Ottawa, ON, K1S 5B6, Canada.

E-mail addresses: jinny.lee@carleton.ca (J. Lee), rthornhill@toh.ca (R.E. Thornhill), pnery@ottawaheart.ca (P. Nery), radekemp@ottawaheart.ca (Robert deKemp), epena@toh.ca (E. Peña), dbirnie@ottawaheart.ca (D. Birnie), andy.adler@carleton.ca (A. Adler), eukwatta@uoguelph.ca (E. Ukwatta).

https://doi.org/10.1016/j.compbiomed.2019.103341
Received 16 February 2019; Received in revised form 20 June 2019; Accepted 20 June 2019

guidance [9]. Areas of abnormal myocardium (‘low bipolar voltage regions’) from fibrotic tissue in the LA are considered as potential targets for ablation [10]. Catheter ablation is an invasive procedure in which radio frequency (RF) energy is delivered through a catheter to deliberately destroy the small regions of heart tissue that are responsible for creating abnormal electrical signals. For example, pulmonary vein (PV) isolation is a common procedure, where the tissue bordering the pulmonary veins (PVs) is targeted for ablation in order to prevent abnormal wave propagation to the rest of myocardium. When electroanatomical voltage mapping (EAM) data is fused with other imaging sources, such as magnetic resonance (MR) Imaging or Computed Tomography (CT), it may provide crucial information for guiding catheter ablation by locating fibrosis.

Together with EAMs, pre-procedural MR can provide a detailed depiction of the LA and the PVs [11]. Late gadolinium enhancement (LGE)-MR is also playing an increasingly important role in the depiction of myocardial fibrosis [12] and can provide potentially relevant information prior to ablation. In late gadolinium enhancement-magnetic resonance imaging (LGE-MRI), images are acquired 10–20 min following a bolus injection of a gadolinium (Gd) based contrast agent, which allows the contrast to distribute to the extravascular-extracellular spaces, and accumulate, in regions of fibrosis. As the use of LGE-MRI increases in pre-ablation planning, there is an urgent need for registration techniques that will enable us to compare the spatial extent of low bipolar voltage areas on EAMs with hyper-enhanced regions on late gadolinium enhancement-magnetic resonance (LGE-MR) images. Several studies have demonstrated that fibrosis regions of the LA detected using LGE-MRI prior to ablation can assist in predicting ablation outcome [13–15]. Leonardi [14] reported that an accurate morphological three-dimensional (3D) left atrial model produced by magnetic resonance imaging (MRI) can improve the cardiac ablation strategy. Romero [15] described the clinical impact of incorporating LGE-MRI data to EAMs, specifically that regions of LGE-MR enhancement may assist in visualizing the fibrosis border zone in the LA.

Although others have reported significant correlations between EAMs and LGE-MRI with respect to the total burden of fibrosis in the LA [16,17], the spatial correlation between regions of low bipolar voltage on EAMs and regions of hyperenhancement on LGE-MRI depends on the accurate alignment of data acquired by these two disparate image modalities (i.e., registration). To our knowledge, registration methods for integration of LGE-MRI and EAMs of the LA have not been adequately described in the literature [18,19]. Therefore, we propose a computational registration and evaluation strategy, which was validated using clinical data acquired from a prospective study of patients with persistent AF.

The primary objective of this work is to develop and validate a registration method for aligning the left atrial surface determined from LGE-MRI to the left atrial surface depicted by EAMs. After implementation of this registration strategy, the secondary objective is to evaluate the spatial correlation between fibrosis depicted in LGE-MRI determined by several segmentation algorithms and regions of low bipolar voltage on EAMs.

2. Materials and methods

2.1. Study subjects and image acquisition

Twenty patients (mean age: 64 years, age range: 45–76 years) participated in this prospective study of persistent AF. The study was approved by the Institutional Human Research Ethics Board, and a written consent was obtained from all participants. 3D LGE-MR images were acquired prior to first-time ablation (median duration: 57 days), and EAMs data were acquired immediately prior to ablation.

All patients underwent MRI examination on a 1.5 Tesla clinical scanner (Siemens Aera, Siemens Medical Systems, Erlangen, Germany). LGE imaging was performed approximately 15 min after injection of 0.1 *mmol/kg* Gadobutrol (Gadovist, Bayer Healthcare, Canada) using a 3D inversion recovery prepared gradient echo sequence. All MR images were ECG gated and acquired during the end-diastolic phase of the respiratory cycle, i.e., LA diastole phase. Participants were instructed to breath freely during image acquisition and respiratory navigator gating was used to ensure consistent data collection during the end-expiration phase of the respiratory cycle. Images were acquired with an inversion time selected to null the signal from normal ventricular myocardium (typically between 340 and 360 *ms*). The 3D images were acquired axially with a voxel size of $1.25 \times 1.25 \times 2.5\, mm^3$, which was subsequently subsampled to $0.625 \times 0.625 \times 1.25\, mm^3$.

Participants underwent voltage mapping prior to cardiac ablation. The protocol was standardized to collect voltage mapping data while the participant was in sinus rhythm (i.e., instead of while in AF). Additionally, the mapping points were acquired at the P-wave during early atrial systole which corresponds to the end-diastolic phase of the left ventricle. A mapping catheter and proximal electrodes accessed the left atrial chamber percutaneously to record the unipolar and bipolar signal [20]. Sequential contact along the left atrial endocardium of the mapping catheter was recorded with respect to its position (vertex), the distance from location sensors to three coil magnetic fields beneath the patient triangulated in space (face), and the magnitude of the local peak voltage at each vertex (uni/bipolar voltage). The CARTO (Biosense Webster, Inc. Irvine, California, USA) workstation progressively displays the reconstruction of the left atrial chamber in 3D space with color encoding of sequential activation time, where purple-to-green denotes healthy myocardium, yellow the border zone, and red fibrosis on the basis of bipolar voltage as shown in Fig. 1 [21].

2.2. Dataset preprocessing

A cardiothoracic radiologist with 7 years of experience manually segmented the left atrial blood-pool and wall on LGE-MR images using the Cardiac MRI Toolkit extension (CARMA Center, University of Utah, UT, USA) in 3D Slicer (www.slicer.org) [22]. For the left atrial blood-pool segmentation, the left atrial appendage and PVs (and their respective ostia) were identified by the operator who then defined five walls (septal, posterior, anterior, inferior, and roof) of the LA. Subsequently, the axial dilate function (Cardiac MRI Toolkit) was applied to the left atrial blood-pool volume. In particular, this function performs a four-pixel radius binary dilation (in-plane) for each two-dimensional (2D) axial slice. A first approximation of the left atrial wall contours was then created by subtracting left atrial blood-pool segmentation from the dilated result; contours were subsequently refined manually by the radiologist (i.e., thinning or thickening the wall as appropriate). We utilized the segmented myocardium of the LA as the region of interest (ROI) for the purpose of registration to EAMs surfaces, and for delineation of fibrosis.

We built a polygonal mesh representing the LA composed of vertices and faces from the label map using the Marching cube algorithm [23]. We also constructed a left atrial surface composed of multiple polygons derived from vertices and faces that were transferred from the EAMs. The coordinates (vertices) were formatted as a matrix, and the triangulation connectivity (faces) was labeled for identifying specific vertices using the triangulation. The preprocessing for both data was performed in Matlab 2017b (The MathWorks, Inc., Natick, Massachusetts, USA).

3. Registration of left atrial surface determined by LGE-MRI to EAMs

3.1. Overview of our approach

In image processing, registration involves aligning two or more objects into the same spatial scene [24]. In this work, we used a point cloud to represent the left atrial geometry, as isolated from LGE-MR

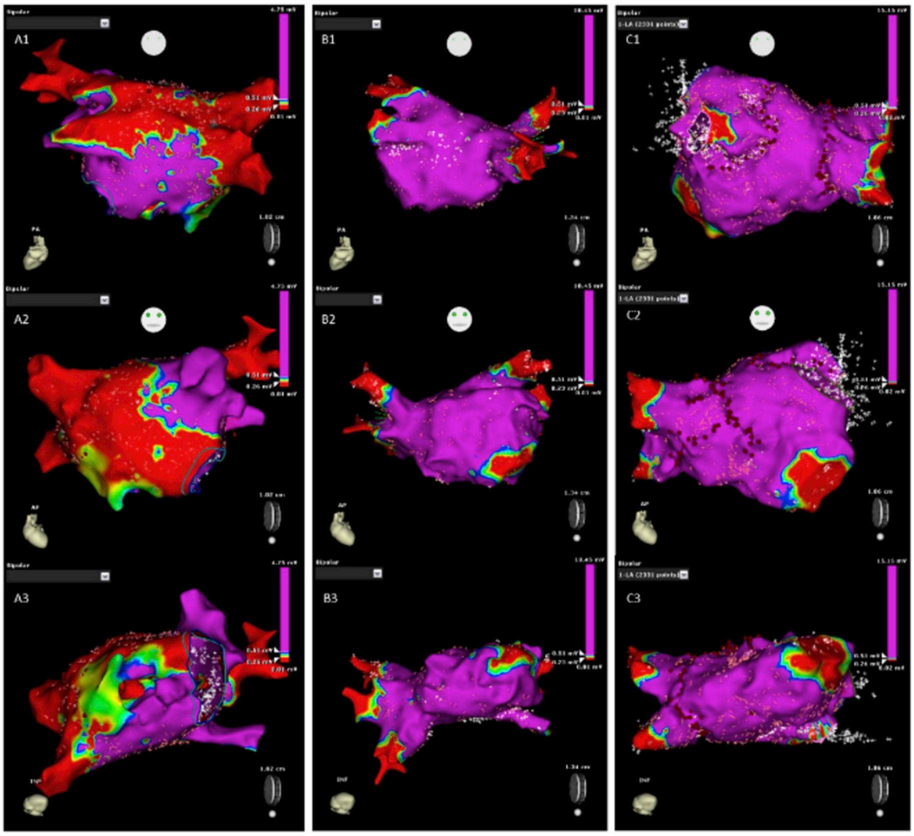

Fig. 1. Examples of EAMs images obtained from 3 representative patients with persistent AF, displayed in gradient color (patients A (left), B (middle), and C (right)). The gradient color bar on the top right shows the geometric bipolar voltage values for each LA; purple-to-green indicates healthy myocardium, whereas red and yellow indicate areas of fibrosis and border-zone, respectively. The red dots adjacent to PVs indicate the recorded locations of ablation ('PV isolation'). Images displayed in the top row correspond to the posterior view of the LA, those in the middle row correspond to the anterior view of the LA, and those on the bottom row correspond to the inferior view of the LA. The images were generated by CARTO XP system viewer version 1.0.0.4.

images and EAMs data. In this context, a point cloud is a collection of coordinate points, $XY(Z)$, in space, which can be converted to create a surface of the LA using Delaunay triangulation.

Our proposed registration pipeline is shown in Fig. 2, which consists of manual, affine, and non-rigid alignments. In the original space (i.e., prior to registration), LGE-MR and EAMs data were located in the same scene of 3D space at a remote distance. In the manual registration step, translation and rotation transformations were applied to relocate the left atrial surface determined from LGE-MRI closer to the EAMs, as guided by the anatomy of the LA. This was followed by application of an iterative closest point (ICP) algorithm, in which the left atrial surface determined by LGE-MRI was deformed to that of EAMs in an affine manner. Finally, we applied a non-rigid ICP (NICP) algorithm to maximize the matching criteria by searching for the correct parameters in a deformation field.

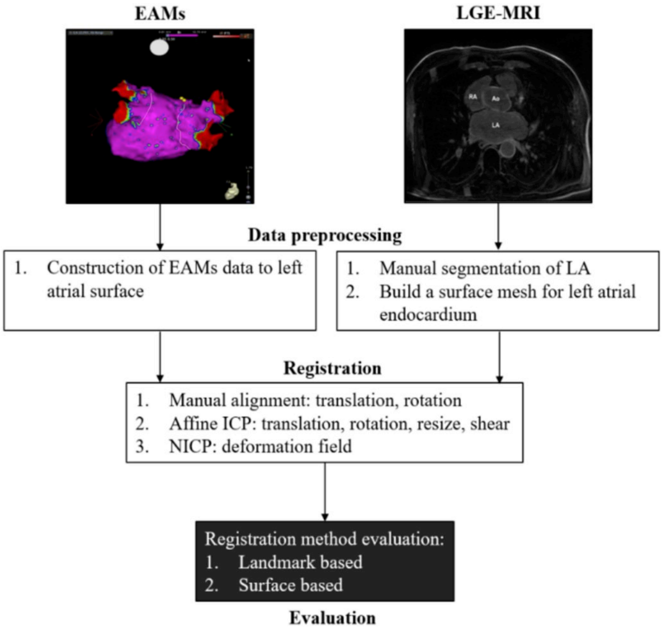

Fig. 2. Point cloud registration flow diagram. The top left image indicates EAMs data and the top right image indicates LGE-MRI data. Both EAMs and LGE-MRI data were preprocessed before registration was performed. The results of the registration were validated by both landmark-based and surface-based evaluation methods.

After registration, we projected the regions of fibrosis as determined by LGE-MRI to the low bipolar voltage regions on EAMs to investigate their spatial correlation, as shown in Fig. 3.

3.2. Manual alignment

In our registration process, we used EAMs as our target and the left atrial point cloud from LGE-MRI as the source, which was ultimately deformed to match the target. We elected to designate EAMs as the target due to its fundamental role in guiding ablation treatment for AF. Furthermore, currently, EAMs was chosen as target due to its dominant treatment tool to treat AF. In this study, LGE-MRI is the cross-sectional imaging modality to find the spatial correlation with low bipolar voltage regions on EAMs. The point cloud for the source (s) is a set of vertices $v^s = (v_1, ..., v_i) \in R^3$ and faces $f^s = (f_1, ..., f_l) \in R^3$, and the point cloud for the target (t) is a set of vertices $v^t = (v_1, ..., v_j) \in R^3$ and faces $f^t = (f_1, ..., f_m) \in R^3$.

We manually aligned the two left atrial surfaces first to provide a good initialization for the ICP algorithm by observing the resultant shortest distance between corresponding landmarks. The source was aligned to the target manually while considering the structure of the LA (e.g., left superior PV (LSPV), left inferior PV (LIPV), right superior PV (RSPV), right inferior PV (RIPV), and the mitral valve). In this step, six degrees of freedom (DOF) were allowed (3 rotations +3 translations)

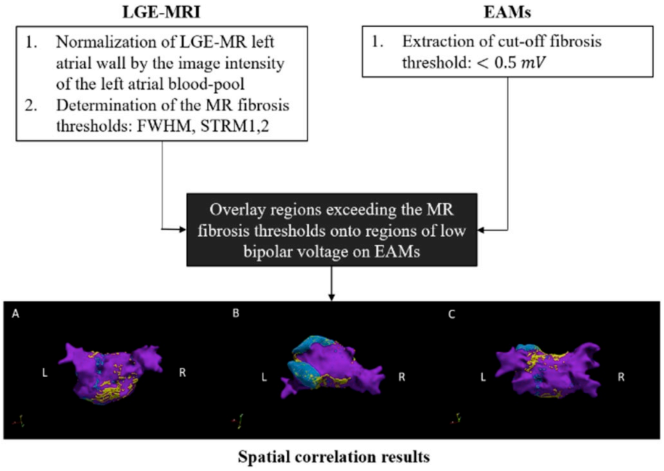

Fig. 3. Projection flow diagram. Both LGE-MRI and EAMs data were preprocessed before projection was performed. Regions of LGE-MR fibrosis were identified using three threshold-based approaches and their correspondence with regions of low bipolar voltage (EAMs) was assessed. In the example of the spatial correlation result (bottom images), A denotes posterior view, B denotes anterior view, C denotes inferior view, and L denotes left, R denotes right. The registered LA was depicted in purple, blue depicts the regions of low bipolar voltage on EAMs, and yellow depicts the distributed gadolinium on LGE-MRI.

for this registration.

3.3. Affine ICP registration

The most popular registration method for point cloud data is the ICP algorithm [25,26]. In the standard ICP algorithm, adjacent points on each point cloud refine their distance at each iteration using translation and rotation transformation matrices. Refined transformation of the output results in minimization of the error metric, e.g., the root mean squared differences, between coordinates from two point clouds. In contrast to the standard ICP algorithm, we applied affine ICP with 12 DOF (3 rotations + 3 translations + 3 scales + 3 shears) to the manually aligned point cloud due to the dissimilar appearance of the source and target. We applied the entire set of vertices from the two point clouds in this step to maintain consistency across each registration step. The rotation was included due to the misalignment of the two point clouds with respect to their initial coordinate locations; shear transformations were applied to the MR data due to its position with slanted angle, and a scaling factor was applied to correct for the volume differences between MR and EAMs data due to the differences in the phase of MR image and EAMs data acquisition. The affine ICP algorithm created uniform grids of target vertices by sorting the points into local groups to speed up the distance measurement process. The source points were then calculated by the radius of each point from the uniform grid. For point correspondence between the two surfaces, the nearest source point from the target grids was found using *k*-dimensional tree method (k-d tree) [27], which is a computationally efficient algorithm to find the nearest point on the other surface. This approach is initiated by calculating the distance of correspondences from the target to source followed by a selection of those with the shortest distance. The error function associated with affine ICP can be written as;

$$E(a) = \sum_{j=1}^{N_{v^t}} w_i(\, min_j(\varepsilon^2(|v_j^t - T(a;\, v_i^s)|))\,) \tag{1}$$

where N_{v^t} is a number of vertices for target, w_i is a weight, min_j is part of minimization process of the distance between target and source, $\varepsilon^2(|x|) = x^2$ is an error function for alignment measurement where $x \in R^3$ is manually aligned vertices of source, v_i^s is a set of vertices for source, T represents a transformation where $a \in R^{12}$ are parameter vectors including translation, rotation, scale, and shear, and v_j^t is a set of vertices for target. We set w_i as zero for vertices with no finding for the corresponding vertex, and one otherwise. During point cloud registration, only vertices were included in the registration procedure. At each iteration, a least squares method was used to reduce the average distance between corresponding points, and the individual distance between corresponding points was reduced.

Considering the large number of vertices (mean v^s: 40,358, mean v^t: 27,684), we used memory efficient optimizers supported by Quasi-Newton, Broyden–Fletcher–Goldfarb–Shanno (BFGS) [28–30], and followed by Davidon-Fletcher-Powell [29]. Quasi-Newton analyzes successive gradient vectors, $\nabla_{v_i^s} F = g(v_i^s)$ where $F(v_i^s)$ is a minimizing function, by updating Hessian matrix;

$$Hessian\ H^* = H - \frac{Hyy^T H}{y^T Hy} + \gamma ss^T \tag{2}$$

where H is an approximation to the inverse Hessian, $s = v_i^{s*} - v_i^s$ and $y = g^* - g$ are the changes in v_i^s and g made at each iteration, T denotes transpose, $*$ denotes an appropriate value to the next iteration, and $\gamma = \frac{1}{y^T s}$.

Using a Quasi-Newton optimizer, the local minimum and maximum can be found by approaching the value of the function tolerance by minimizing the distance error. The BFGS formula is used here;

$$B^* = (I - \gamma ys^T)B(I - \gamma sy^T) + \gamma yy^T \tag{3}$$

where I is an approximate Hessian matrix, and B is a positive definite Hessian matrix. In this context, vector s^T and y must satisfy the curvature condition;

$$s^T y \;=\; s^T Bs \;>\; 0 \tag{4}$$

3.4. Non-rigid ICP registration

As the deformation of the heart muscle is non-linear, we also applied a non-rigid registration of EAM data to the MR point cloud which underwent affine ICP after manual alignment. We used a NICP algorithm that is similar to the one described by Amberg [31]. We retained a locally affine regularization, smooth translation, and set the number of iterations for all datasets as 160 based on previous study [31]. In our implementation of NICP, we used the quadratic cost function [32] for the minimization of distances between the deformed source and the target. This can lead us to solve the minimization problem directly and exactly due to more than three parameters per vertex in the deformation field. The affine 3 × 4 transformation matrix X_p is predefined for each vertex of the source, and the error function in NICP is;

$$E_d(X) \approx \sum_{v_i \in s} w_p\,(dist^2(t,\, X_p v_i^s)) \tag{5}$$

where $X := [X_1 \cdots X_p]^T$ is an affine matrix, X describes a set of displaced source vertices, $v_i = [x, y, z, 1]^T$ is homogenous coordinates, s denotes source, w_p is a weight, t is a target, and $dist(t, v_i^s)$ denotes a distance between a source point v_i^s and its closest point on the target surface. We set w_p as zero for vertices where no finding for the corresponding vertex, and w_p as one for other vertices. We included an additional regularization function [32] by penalizing the adjacent vertices of the source to be mapped to the disparate vertices of the target in transformation. The error function is used;

$$E_r(X) \approx \sum_{\{v_i^s,\, v_j^t\} \in E^t} \|(X_j - X_i)G\|_F^2 \tag{6}$$

where E^t denotes edges of target, X_j and X_i are affine transformation matrix for target and source, G is a weighting matrix by $G = diag(1,1,1,\gamma)$, γ used as differences in weighting in rotational deformation, set to one here, and was scaled into the $[-1,\ 1]^3$ cube. $\|\cdot\|_F$ is Frobenius norm.

The complete objective function (E) for cost function is the weighted sum of the two-error functions by;

$$E(X) \approx E_d(X) + \alpha E_r(X) \tag{7}$$

where $\alpha = 1,\ \alpha^q > \alpha^{q+1}$, is a weight for smoothness of source and it was lowered when two successive iterations (i.e., q) were smaller than a threshold.

4. Segmentation of fibrosis in LGE-MRI

In this study, we applied the image intensity normalization method advanced by Giannakidis [33]. We normalized the image intensity of the voxels within the left atrial wall contours by that of the left atrial blood-pool [33] using the following;

$$NI(h) = [I(h) - \mu_{bp}]/\sigma_{bp} \tag{8a}$$

where $NI(h)$ is normalized left atrial wall intensity, μ_{bp} is the mean value of the left atrial blood-pool signal I, σ_{bp} is the standard deviation value of left atrial blood-pool signal I, and $I(h)$ is left atrial wall intensity for each voxel, h. Both μ_{bp} and σ_{bp} were computed from the image intensity histograms corresponding to the left atrial blood-pool (Fiji open source software, National Institutes of Health, MD, USA).

We applied three different methods for identifying voxels in left atrial wall as "fibrosis" for the purpose of finding a spatial correlation with low bipolar voltage regions on EAMs. The full width half maximum (FWHM) method labels voxels with normalized signal intensity greater than half the maximum signal intensity within a hyper-enhanced region as fibrosis. The voxels with signal intensity greater than the mean + 1 standard deviation intensity of the left atrial wall are defined as fibrotic in STRM1, and the voxels with signal intensity greater than the mean + 2 standard deviation intensities of the left atrial wall are defined as fibrotic in STRM2.

5. Spatial correlation of fibrosis determined by LGE-MRI to low bipolar voltage regions on EAMs

We projected vertices labeled as fibrosis in the left atrial wall determined from LGE-MR, created using intensity-threshold-based techniques, on EAMs to evaluate their spatial correlation. We used k-d tree method [34] based on the Euclidean distance (ED) metric to locate the closest point on the target surface. In the Euclidean space, the minimum distance between two points is drawing a straight line. During k-d tree search, each vertex of fibrosis in the left atrial wall was regarded as a query point and unlabeled points (vertices in the registered left atrial endocardial surface of LGE-MR) were classified to query points under the ED metric. Subsequently, we limited our assessment of fibrosis in the LA on MR to the registered left atrial endocardial point cloud delineated by the ROI, i.e., to the exclusion of tissue directly adjacent to the PVs. Next, we determined the cut-off value (below 0.5 mV) [35,36] for the regions of low bipolar voltage on EAMs for the purpose of discovering a spatial relationship with LGE-MR. Accordingly, each vertex corresponding to the three fibrosis thresholds on LGE-MR (FWHM, STRM1, and STRM2) was projected to the regions of low bipolar voltage on EAMs. The resultant LGE-MR-to-EAMs projections were displayed using ParaView open source software (Kitware Inc., New York, NY, USA).

We identified areas of potential spatial correlation between LGE-MRI and EAMs by searching for LGE-MR fibrotic vertices that were located within a 3 mm radius of the EAMs low bipolar voltage vertices which we arbitrarily set based on the normalized Euclidean distance (NED) measurement. The NED defines the squared distance between two point sets with uniformed scale form [37].

6. Comparison of our method to a state-of-the-art technique

We compared results of our method to the coherent point drifts (CPD) [38], which is an alternative to the NICP algorithm. We selected the CPD algorithm inspired by Liang [39] as a comparison to our NICP algorithm. The CPD algorithm considers the alignment of target and source datasets as a probability density estimation problem and coherently re-parameterizes Gaussian mixture model centroid locations with rigid parameters using maximization step of the Expectation-maximization algorithm. The CPD algorithm followed the same procedure for registration up to affine ICP. No more than 50 iterations were set for convergence due to its demands on memory.

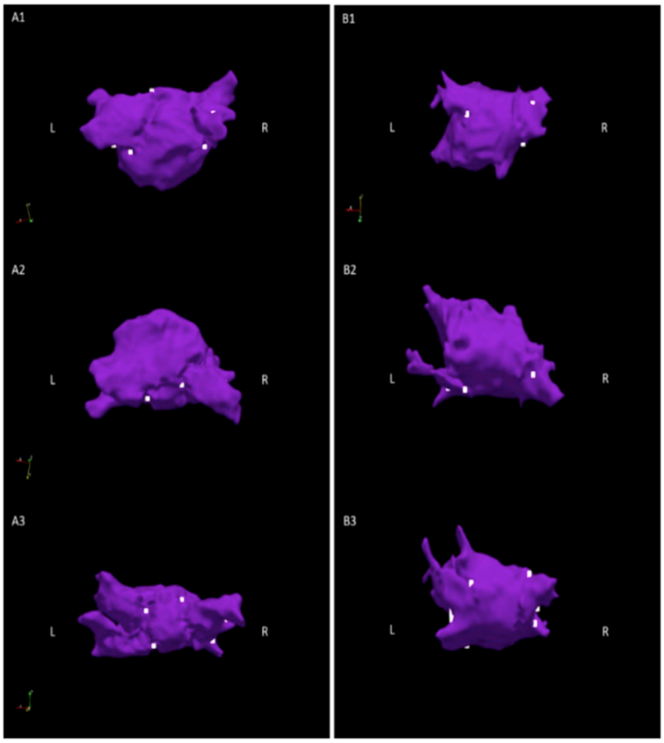

Fig. 4. Example of the location of the eight landmarks in the LA with three points of view, displayed in white square dots (patients A (left), B (right)). (1) Posterior view, (2) Anterior view, (3) Inferior view. A total of eight landmarks were selected, and two points at each PV are located at a diagonal direction in the middle of a short (or long) vestibule or funnel-like common vein in PVs. 'R' and 'L' denote right and left, respectively.

7. Evaluation of our registration approach

We used a landmark-based evaluation method by measuring the distance between corresponding landmark points on the two surfaces in ParaView. Fig. 4 shows the location of the chosen landmarks. To choose distinctive features in the LA, two vertices in the diagonal direction at each PV were selected under careful visual inspection. For left PVs, in the middle of a short vestibule or funnel-like common vein between LSPV and LIPV, the adjacent edges of the posterior and anterior wall were chosen as landmarks. Similarly, in the middle of a long vestibule between RSPV and RIPV, the edges on the right PV areas were selected as landmarks. We did not use the mitral valve as a landmark due to the obscurity of its position on EAMs. As the target object, the landmarks on EAMs are static whereas the corresponding point on MR was selected one by one manually for each registration step. We used target registration error (TRE)

$$TRE(v^t, v^s) = \sqrt{\frac{1}{8}\sum_{k=1}^{8}(v_k^t - v_k^s)^2} \tag{8b}$$

as the metric for evaluating the registration method, where k is the number of landmarks.

We also validated our registration method by computing the alignment of the entire surface of point pair correspondence. We computed the distance from all vertices in EAMs to those in MR based on the ED metric, and vice versa. Then, the median value (*M*) of the results at each coordinate was selected as the distance between EAMs and LGE-MRI. The evaluation results are presented as medians and interquartile ranges due to the non-Gaussian distribution of the ED measurement. The distance computation of surface-based evaluation was followed by;

$$d(v^t, v^s) = M\sqrt{(v^t - v^s)^2} \qquad (9)$$

All statistical analyses were conducted using the SAS environment (SAS Institute Inc., Cary, NC, USA). Differences in the ED measurement (surface-based evaluation) from the manual-alignment to affine ICP, and finally to NICP were assessed using a non-parametric repeated measure (Friedman) test. Post-hoc Wilcoxon paired tests were performed to assess pair-wise differences between manual-alignment and affine ICP, manual-alignment and NICP, and affine ICP and NICP, and NICP and CPD with respect to TRE (landmark-based evaluation). Afterward, we validated the performance of CPD with our evaluation methods. The mean number of iterations and running time for affine ICP, NICP, and CPD were also compared. A p-value <0.05 was considered statistically significant.

The spatial correlation of fibrosis on LGE-MRI with low bipolar voltage regions on EAMs was evaluated by deriving the following from a 2 × 2 contingency table;

- Sensitivity = TP/(TP + FN),
- Specificity = TN/(TN + FP),
- Precision = TP/(TP + FP), and
- Accuracy = (TP + TN)/(TP + FP + TN + FN).

where TP represents the number of true positives, i.e., the fibrosis vertices for source within 3 *mm* of NED of the low bipolar voltage vertices for target, FP represents the number of false positives, i.e., the non-fibrosis vertices for source within 3 *mm* of NED of low bipolar voltage vertices for target, TN represents the number of true negatives, i.e., the non-fibrosis vertices for source within 3 *mm* of NED of the high bipolar voltage (>0.5 mV) vertices for target, and FN represents the number of false negatives, i.e., the non-fibrosis vertices for source within 3 *mm* of NED of the low bipolar voltage vertices for target.

8. Results

We summarized the results of our landmark-based TRE for our method and the alternative method (CPD) in Table 1. Manual alignment reduced the TRE from 368.94 *mm* to 25.06 *mm*, which was decreased further to 20.97 *mm* after affine ICP (Wilcoxon paired test between manual alignment and affine ICP, $p < 0.05$). NICP improved the TRE to 0.61 *mm* whereas CPD only improved the TRE to 1.8 *mm* (Wilcoxon paired test between NICP and CPD, $p < 0.01$). The TRE reduction associated with the NICP step was significantly greater than that which was achieved by affine ICP (A reduction of 0.61 *mm* for NICP vs. 20.97 mm for affine ICP, $p < 0.01$). The proposed registration outperformed the CPD algorithm in terms of TRE by three-fold, based on landmark evaluation. The median ED measurements associated with each registration step are depicted in Fig. 5.

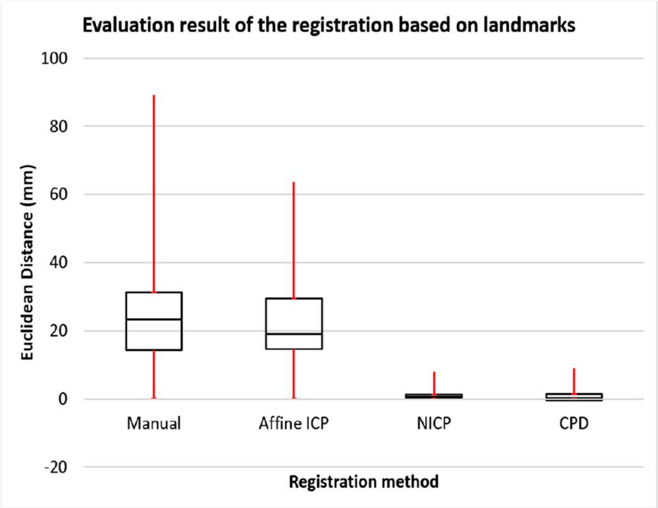

Fig. 5. Median and quartile ranges for the ED are depicted for manual, affine ICP, NICP, and CPD registration.

The surface-based evaluation of registration accuracy is presented in Fig. 6. Similar to the results of landmark-based evaluation, the proposed evaluation method resulted in a three-fold improvement in registration accuracy for NICP compared to the CPD algorithm.

Table 2 shows the number of iterations and computational time required to perform affine ICP, NICP, and CPD registration methods. The number of iterations varied due to the convergence threshold configuration ($\tau > 0$) for affine ICP whereas NICP and CPD were set as static value due to complete utilization of vertices for the source. Affine ICP (0.39 ± 0.24 *min*) demonstrated a fast execution time, particularly relative to the running time required for our NICP registration steps (79 ± 16.73 *min*), using a workstation with an Intel *i7* processor and a memory of 12 GB. In a similar fashion, CPD algorithm considerably increased the computational time (21 *hrs* 27 *min* ± 19 *hrs* 44 *min*), an increase of sixteen-fold compared to NICP.

Fig. 7 depicts the spatial correlation between two surfaces in a qualitative manner for FWHM, STRM1, and STRM2. In general, the regions of low bipolar voltage on EAMs are denser and more tightly clustered than the regions of hyperenhancement on LGE-MRI. STRM1 demonstrated the highest density of fibrosis on LGE-MRI, and followed by FWHM and STRM2. Table 3 summarizes the extent of spatial correlation between regions of hyperenhancement delineated by LGE-MRI and low bipolar regions on EAMs. Overall, all three methods for fibrosis detection demonstrated over 80% accuracy, and over 90% specificity. STRM1 showed the highest values of sensitivity (41.31%) and precision (90.6%) whereas FWHM and STRM2 showed much lower values of sensitivity (7.6% and 2.78%) and slightly lower values of precision (69.27% and 78.68%).

Table 1
Evaluation result of the registration method based on landmarks using the ED measurement (*mm*). Q1 denotes 1st quartile, Q3 denotes 3rd quartile, IQR denotes interquartile, and SD denotes standard deviation. Optimal results are shown in bold.

Registration step/(*mm*)	Mean	Median	Min	Max	IQR (Q1-Q3)	SD	Outliers (low)	Outliers (high)
Original	365.77	368.94	206.6	473.47	337.2–403.85	54.64	6	160
Manual	26.73	25.06	1.74	90.95	16.09–33.04	15.47	0	153
Affine ICP	21.99	20.97	1.99	104.55	16.67–31.44	11.00	0	157
NICP	**0.86**	**0.61**	**0.05**	**8.02**	**0.41–1.26**	**0.9**	**0**	**151**
CPD	2.25	1.80	0.26	8.67	1.10–3.14	1.59	0	155

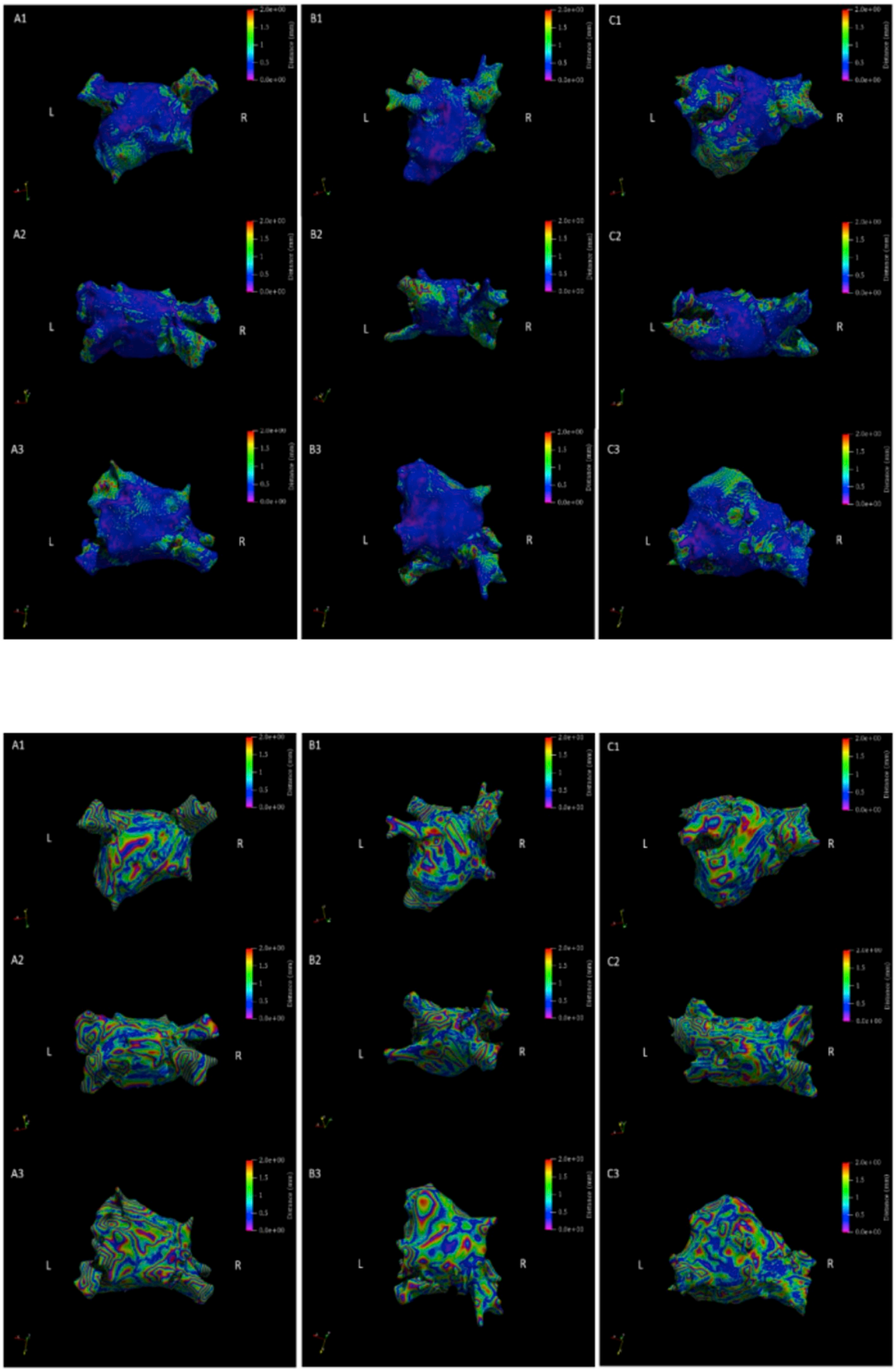

Fig. 6. Representative distance maps depicting the results of NICP registration method (top) and CPD registration method (bottom) based on the surface evaluation using the entire vertices on LGE-MRI and those on EAMs for patients A (left), B (middle), and C (right). (1) Posterior view, (2) Anterior view, (3) Inferior view. The distance maps were depicted in a gradient color bar at the top right ranged from 0 to 2 mm. All measurements are depicted in *mm*.

Table 2
The number of iterations and computation time required for affine ICP, NICP, and CPD. CT denotes computational time in seconds.

Registration Iteration/CT	Affine ICP iteration	Affine ICP CT (sec)	NICP iteration	NICP CT (sec)	CPD Iteration	CPD CT (sec)
Mean	33	23.1	160	4739.6	50	77265.3
Min	15	2.0	160	1557.4	50	1190.0

9. Discussion

The objective of this study was to develop and evaluate a method for registering the left atrial surface from EAMs to the one determined from LGE-MR images. Such a method would enable the merging of complementing information from both LGE-MRI with EAMs, and potentially assist with ablation strategies for patients with AF. We described a registration pipeline based on the ICP algorithm, which was evaluated by measuring distance between manually picked anatomical landmarks in left atrial surface obtained from both EAMs and LGE-MRI. In our approach, the ICP algorithm was used to deform the left atrial surface

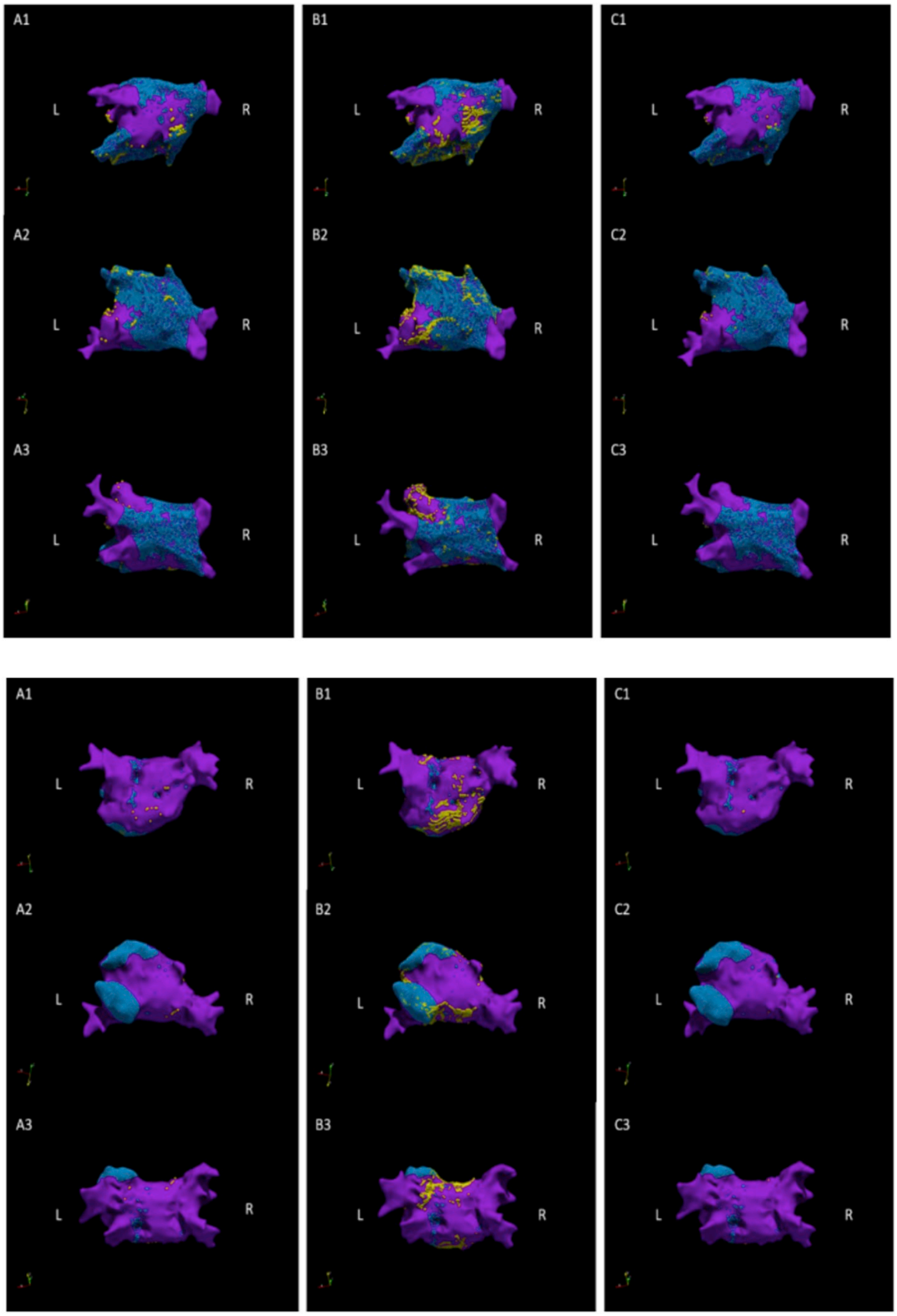

Fig. 7. Representative results from two patients (top, bottom) depicting the spatial correlation between regions of low bipolar voltage on EAMs and regions of hyperenhancement on LGE-MRI using each of the three thresholds for left atrial fibrosis. The regions of low voltage on EAMs is stationary whereas fibrosis on LGE-MRI differs due to fibrosis thresholds. (1) Posterior view, (2) Anterior view, (3) Inferior view; (A) FWHM, (B) STRM1, (C) STRM2. Regions depicting low bipolar voltage on EAMs are shown in blue, while regions of hyperenhancement on LGE-MR are shown in yellow.

Table 3
Results of a relationship between the regions of fibrosis on LGE-MRI and the regions of low bipolar voltage on EAMs.

Method	Sensitivity (%)	Specificity (%)	Precision (%)	Accuracy (%)
FWHM	7.6	99.9	69.27	83.21
STRM1	41.31	99.33	90.6	85.05
STRM2	2.78	99.92	78.68	84.05

determined using LGE-MRI to that of EAMs by an affine transformation; we then applied a NICP to deform the left atrial surface by non-linear deformations. The results demonstrated that NICP can provide significant incremental improvement over the use of affine ICP alone (median TRE $20.97\,mm$ in affine ICP vs. $0.61\,mm$ in NICP). Furthermore, NICP outperformed the results reported by previous studies (mean TRE for left ventricle: $3.41-3.8\,mm$[18,19], LA: $>5\,mm$ [40]), in terms of the accuracy of registration assessed by points-based methods.

Our evaluation of a non-rigid algorithm for registration provides background information to clinical studies requiring the spatial correlation of fibrosis with low-voltage points on EAMs. Although several studies [18,19,41] have evaluated the correlation of two surfaces by computing a global assessment of fibrosis correlation (i.e., over the entire left atrial wall), there has been a dearth of studies focused on evaluating the potential algorithms for registration. The spatial correlation between fibrosis determined by MRI to low bipolar voltages on EAMs based on our registration method demonstrated over 80% in accuracy for all fibrosis thresholds, with the best accuracy achieved by the STRM1 intensity threshold. Low sensitivity was expected due to the disparate mechanisms of identifying "fibrosis" with each imaging technique: while the accumulation of gadolinium and associated T1 shortening reflects an expansion and disruption of the extravascular-extracellular space on LGE-MRI, the low bipolar voltage regions on EAMs are thought to result from electrical remodeling, autonomic nervous system changes, or calcium handling abnormalities [42]. Conversely, the specificity of each threshold for identifying EAMs-positive low-voltage regions was high due to the preponderance of unenhanced regions on LGE-MRI.

Our study has several limitations. First, the cohort consisted of only 20 patients, which was relatively small. Despite the small number of patients, we demonstrated statistically significant improvements in registration performance metrics using non-parametric repeated measures (Friedman and Wilcoxon paired tests).

Importantly, the MR image resolution greatly influences the ability of the imaging technique in identifying the fibrotic regions, as the left atrial wall is very thin. As we acquired contiguous 3D spatial data via multi-slice selection, this leads to anisotropic spatial resolution, especially in the *z* direction. In terms of the signal intensity, acquired image contrast under LGE-MRI relies normally on the signal intensity difference between healthy myocardium and myocardial fibrosis. Although LGE-MR images are designed to delineate healthy from fibrotic myocardium, there is not always a clear differentiation between fibrosis and adjacent normal myocardium. In the same manner, the assessment of diffuse myocardial fibrosis can be ambiguous in terms of defining the threshold of fibrotic tissue. Moreover, the extent of hyperenhancement may differ depending on the signal intensity threshold selected by the operator or image analyst. Finally, irregular heart-rates or respiratory rates can heavily impact LGE-MR image quality.

The ICP algorithm is considerably influenced by the initial alignment. Despite careful manual alignment, this factor can influence the outcome of the registration, and ultimately the degree (strength) of the spatial relationship between hyper-enhanced regions on LGE-MRI and low bipolar voltage regions on EAMs. Further automation could be achieved by replacing the manual alignment step with an alternative approach, wherein the center of gravity of the LA is used to initialize the alignment of the two point clouds. Advanced refinement [43] of the ICP algorithm, e.g., uniformed sub-sampling of the available points, random sampling with different points at each iteration, a large number of normal among selected points, can be further studied to improve the accuracy of the registration. With respect to NICP, the computational time can be greatly reduced if a small number of iterations can provide similar results. To improve computational time of the registration method, faster program environment, e.g., C, or simplified structure of the registration algorithm can be alternative options.

With respect to dataset preprocessing, manual segmentation of the left atrial wall was a considerably time-intensive task, which is subject to high observer variability. The application of automatic segmentation methods can be studied in the future to improve the computational time of registration further. For instance, principal component analysis may be performed on the left atrial shapes on LGE-MRI, and then align them based on eigenvectors to those of EAMs. Yang [44] proposed a model-based method to segment LA with left atrial appendage and PV trunks from CT images using marginal space learning, and obtained over 0.94 outcome based on Dice's coefficient evaluation. Veni [45] presented a surface-detection method of segmenting LA by computing a—posterior estimate and obtained over 0.9 in Dice's coefficient.

Finally, due to the properties of EAMs, regions of hyperenhancement in the left atrial wall of LGE-MRI was projected to the constructed left atrial endocardium depicted in EAMs by finding the shortest path (straight line), where their corresponding point should be computed over the surface of the LA, i.e., geodesic distance. Although we used the ED measurement for its wide-usage and simplicity, another disadvantage with the ED is the largest-scaled features dominate the others if dataset clusters are not isolated or compacted [46]. An alternative metric can be proposed to refer to the shortest path between two vertices on a curved surface or sphere.

10. Conclusions

We developed and validated a method for registering the left atrial surface on LGE-MRI to one on EAMs based on three integration steps. The results demonstrated that the integration of left atrial point cloud outperformed the comparative method verified by our evaluation methods. Furthermore, a substantial correlation between low bipolar voltage regions on EAMs and hyper-enhanced regions on LGE-MRI was demonstrated. The development of registration and evaluation methods can be utilized to compare EAMs to data obtained from cross-sectional imaging modalities such as CT or MR. Refinement of these methods will lead to valuable tools for the identification of arrhythmogenic foci that might be otherwise missed during cardiac ablation, and therefore improve outcomes for patients with persistent AF.

Disclosure of conflicts of interest

The authors have no relevant conflicts of interest to disclose.

Acknowledgements

Funding for this study was supported by Natural Sciences and Engineering Research Council of Canada (NSERC) Discovery Grant and the Cardiac Arrhythmia Network of Canada (CANet) Strategic Research Grant program (SRG-15-P06-001) as part of the Networks of Centres of Excellence of Canada. The author is a member of the Cardiac Arrhythmia Network of Canada (CANet) HQP Association for Trainees (CHAT). The authors gratefully acknowledge the technical contributions of Sophie Chenier, MRT, and Owen Clarkin, PhD.

References

[1] E.J. Benjamin, Heart disease and stroke Statistics'2017 update, A Report from the American Heart Association vol. 135, (2017), https://doi.org/10.1161/CIR.0000000000000485.

[2] V. Fuster, Acc/aha/esc 2006 guidelines for the management of patients with atrial fibrillation: a report of the American college of cardiology/American heart association task force on practice guidelines and the European society of cardiology committee for practice, Circulation 114 (7) (2006) e257–e354, https://doi.org/10.1161/CIRCULATIONAHA.106.177292.

[3] H. Calkins, HRS/EHRA/ECAS EXPERT CONSENSUS STATEMENT 2012 HRS/EHRA/ECAS expert consensus statement on catheter and surgical ablation of atrial fibrillation: recommendations for patient selection, procedural techniques, patient management and follow-up, Definitions, E. *Eur Niv Ad.* 14 (2012) 528–606, https://doi.org/10.1093/europace/eus027.

[4] A. Verma, Approaches to catheter ablation for persistent atrial fibrillation, N. Engl. J. Med. 372 (19) (2015) 1812–1822, https://doi.org/10.1056/NEJMoa1408288.

[5] P.G. Platonov, L.B. Mitrofanova, V. Orshanskaya, S.Y. Ho, Structural abnormalities in atrial walls are associated with presence and persistency of atrial fibrillation but not with age, J. Am. Coll. Cardiol. 58 (21) (2011) 2225–2232, https://doi.org/10.1016/j.jacc.2011.05.061.

[6] T. Kazui, M.C. Henn, Y. Watanabe, The impact of weeks of atrial fibrillation on left atrial and ventricular structure and function, J. Thorac. Cardiovasc. Surg. 150 (6) (2018) 1602–1608, https://doi.org/10.1016/j.jtcvs.2015.08.105 e1.

[7] A. Verma, Pre-existent left atrial scarring in patients undergoing pulmonary vein antrum isolation: an independent predictor of procedural failure, J. Am. Coll. Cardiol. 45 (2) (2005) 285–292, https://doi.org/10.1016/j.jacc.2004.10.035.

[8] D. Kim, H. Ahn, Current Status and Future of Cardiac Mapping in Atrial Fibrillation, InTech, 2002, pp. 93–124.

[9] D. Bhakta, J.M. Miller, Principles of electroanatomic mapping, Indian Pacing Electrophysiol. J. 8 (1) (2008) 32–50, https://doi.org/10.1056/NEJMoa062800.

[10] K. Nademanee, A new approach for catheter ablation of atrial fibrillation: mapping of the electrophysiologic substrate, J. Am. Coll. Cardiol. 43 (11) (2004) 2044–2053, https://doi.org/10.1016/j.jacc.2003.12.054.

[11] J. Cates, Computational shape models characterize shape change of the left atrium in atrial fibrillation, Clin. Med. Insights Cardiol. 8 (S1) (2014) 99–109, https://doi.org/10.4137/CMC.S15710.

[12] S. Roujol, Improved multimodality data fusion of late gadolinium enhancement MRI to left ventricular voltage maps in ventricular tachycardia ablation, IEEE Trans. Biomed. Eng. 60 (5) (2013) 1308–1317, https://doi.org/10.1109/TBME.2012.2233738.

[13] A. D 'silva, M. Wright, Advances in imaging for atrial fibrillation ablation, Radiol. Res. Pract. 10 (2011), https://doi.org/10.1155/2011/714864.

[14] R. Leonardi, Volumetric identification of left atrial fibrosis from delayed enhancement magnetic resonance imaging in atrial fibrillation: preliminary results, Comput. Cardiol. 41 (2014) 101–104.

[15] J. Romero, CMR imaging for the evaluation of myocardial stunning after acute myocardial infarction: a meta-analysis of prospective trials, Eur. Heart J. Cardiovasc. Imag. 14 (11) (2013) 1080–1091, https://doi.org/10.1093/ehjci/jet040.

[16] R.S. Oakes, Detection and quantification of left atrial structural remodeling with delayed-enhancement magnetic resonance imaging in patients with atrial fibrillation, Circulation 119 (13) (2009) 1758–1767, https://doi.org/10.1161/CIRCULATIONAHA.108.811877.

[17] T.J. Badger, Evaluation of left atrial lesions after initial and repeat atrial fibrillation ablation; Lessons learned from delayed-enhancement MRI in repeat ablation procedures, Circ. Arrhythmia Electrophysiol. 3 (3) (2010) 249–259, https://doi.org/10.1161/CIRCEP.109.868356.

[18] D. Andreu, Integration of 3D electroanatomic maps and magnetic resonance scar characterization into the navigation system to guide ventricular tachycardia ablation, Circ. Arrhythmia Electrophysiol. 4 (5) (2011) 674–683, https://doi.org/10.1161/CIRCEP.111.961946.

[19] A.P. Wijnmaalen, Head-to-head comparison of contrast-enhanced magnetic resonance imaging and electroanatomical voltage mapping to assess post-infarct scar characteristics in patients with ventricular tachycardias: real-time image integration and reversed registration, Eur. Heart J. 32 (2011) 104–114, https://doi.org/10.1093/eurheartj/ehq345.

[20] P.A. Friedman, Novel mapping techniques for cardiac electrophysiology, Heart 87 (April 2005) (2002) 575–582, https://doi.org/10.1136/heart.87.6.575.

[21] D. Corrado, Three-dimensional electroanatomic voltage mapping increases accuracy of diagnosing arrhythmogenic right ventricular cardiomyopathy/dysplasia, Circulation 111 (23) (2005) 3042–3050, https://doi.org/10.1161/CIRCULATIONAHA.104.486977.

[22] A. Fedorov, 3D slicer as an image computing platform for the quantitative imaging Network, Magn. Reson. Imaging 30 (9) (2012) 1323–1341, https://doi.org/10.1016/j.mri.2012.05.001.

[23] W.E. Lorensen, H.E. Cline, Marching cubes: a high resolution 3D surface construction algorithm, Proc 14th Annu Conf Comput Graph Interact Tech vol. 21, SIGGRAPH '87, 1987, pp. 163–169, https://doi.org/10.1145/37401.37422 4.

[24] Z. Xiong, Y. Zhang, A critical review of image registration methods, Int. J. Image Data Fusion 1 (2) (2010) 137–158, https://doi.org/10.1080/19479831003802790.

[25] P.J. Besl, A method for registration of 3-D shapes, IEEE Trans. Pattern Anal. Mach. Intell. 14 (2) (1992) 239–256.

[26] Y. Chen, G. Medioni, Object modeling by registration of multiple range images, Proceedings 1991 IEEE int conf robot autom. 10 1992, pp. 145–155, , https://doi.org/10.1109/ROBOT.1991.132043 3.

[27] D.A. Simon, M. Hebert, T. Kanade, Techniques for fast and accurate intrasurgical registration, Comput. Aided Surg. 1 (1) (1995) 17–29, https://doi.org/10.3109/10929089509106822.

[28] D. Goldfarb, A family of variable-metric methods derived by variational means, Mathematics of Computation, 1970, pp. 23–26, , https://doi.org/10.1090/S0025-5718-1970-0258249-6.

[29] R. Fletcher, M.J.D. Powell, A rapidly convergent descent method for minimization, Comput. J. 6 (2) (1963) 163–168, https://doi.org/10.1093/comjnl/6.2.163.

[30] D.F. Shanno, Conditioning of quasi-Newton methods for function minimization, Math. Comput. 24 (1970) 647–656, https://doi.org/10.1090/S0025-5718-1970-0274029-X.

[31] B. Amberg, S. Romdhani, T. Vetter, Optimal step nonrigid ICP algorithms for surface registration, 2007 IEEE conf comput vis pattern recognit, 2007, pp. 1–8.

[32] B. Allen, B. Curless, Z. Popović, The space of human body shapes, ACM Trans. Graph. (2003), https://doi.org/10.1145/882262.882311.

[33] A. Giannakidis, Rapid automatic segmentation of abnormal tissue in late gadolinium enhancement cardiovascular magnetic resonance images for improved management of long-standing persistent atrial fibrillation, Biomed. Eng. Online 14 (88) (2015), https://doi.org/10.1186/s12938-015-0083-8.

[34] R.F. Sproull, Refinements to nearest-neighbor searching in k-dimensional trees, Algorithmica 6 (1–6) (1991) 579–589, https://doi.org/10.1007/BF01759061.

[35] K. Soejima, W.G. Stevenson, W.H. Maisel, J.L. Sapp, L.M. Epstein, Electrically unexcitable scar mapping based on pacing threshold for identification of the reentry circuit isthmus: feasibility for guiding ventricular tachycardia ablation, Circulation 106 (13) (2002) 1678–1683.

[36] K. Yoshida, Feasibility of targeting catheter ablation to the markedly low-voltage area surrounding infarct scars in patients with post-infarction ventricular tachycardia, Circ. J. 72 (7) (2008) 1112–1119, https://doi.org/10.1253/circj.72.1112.

[37] M.R. Berthold, F. Höppner, On Clustering Time Series Using Euclidean Distance and Pearson Correlation, (2016).

[38] A. Myronenko, X. Song, Point set registration: coherent point drifts, IEEE Trans. Pattern Anal. Mach. Intell. 32 (12) (2010) 2262–2275, https://doi.org/10.1109/TPAMI.2010.46.

[39] L. Liang, M. Wei, A. Szymczak, Nonrigid iterative closest points for registration of 3D biomedical surfaces, Optic Laser. Eng. 100 (2018) 141–154, https://doi.org/10.1016/j.optlaseng.2017.08.005.

[40] Z. Ling, The association of left atrial low-voltage regions on electroanatomic mapping with low attenuation regions on cardiac computed tomography perfusion imaging in patients with atrial fibrillation, Heart Rhythm 12 (5) (2015) 857–864, https://doi.org/10.1016/j.hrthm.2015.01.015.

[41] B.R. Parmar, Comparison of left atrial area marked ablated in electroanatomical maps with scar in MRI, Journal of Cardiovascular Electrophysiology, 2014, https://doi.org/10.1111/jce.12357.

[42] P.B. Nery, R. Thornhill, G.M. Nair, E. Pena, C.J. Redpath, Scar-based catheter ablation for persistent atrial fibrillation, Curr. Opin. Cardiol. 32 (1) (2017) 1–9, https://doi.org/10.1097/HCO.0000000000000349.

[43] S. Rusinkiewicz, M. Levoy, Efficient Variants of the ICP Algorithm, (2001), pp. 145–152.

[44] D. Yang, Y. Zheng, M. John, Graph Cuts Based Left Atrium Segmentation Refinement and Right Middle Pulmonary Vein Extraction in C-Arm CT vol. 8669, (2013), pp. 1–9, https://doi.org/10.1117/12.2007137.

[45] G. Veni, Z. Fu, S.P. Awate, R.T. Whitaker, Bayesian Segmentation of Atrium Wall Using Globally-Optimal Graph Cuts on 3D Meshes, (2013), pp. 656–667.

[46] A.S. Shirkhorshidi, S. Aghabozorgi, T. Ying Wah, A Comparison study on similarity and dissimilarity measures in clustering continuous data, PLoS One 10 (12) (2015) 1–20, https://doi.org/10.1371/journal.pone.0144059.